# Segmentation of Neural Stem/Progenitor Cells Nuclei within 3-D Neurospheres

Weimiao Yu[1], Hwee Kuan Lee[1], Srivats Hariharan[2], Shvetha Sankaran[2], Pascal Vallotton[3], and Sohail Ahmed[2]

[1] Bioinformatics Institute, #07-01, Matrix, 30 Biopolis Street, Singapore 138671
[2] Institute of Medical Biology, #06-06, Immunos, 8A Biomedical Grove, Singapore 138648
[3] CSIRO Mathematical and Information Sciences, Locked Bag 17, North Ryde, NSW, 1670, Australia

**Abstract.** Neural stem cells derived from both embryonic and adult brain can be cultured as neurospheres; a free floating 3-D aggregate of cells. Neurospheres represent a heterogenous mix of cells including neural stem and progenitor cells. In order to investigate the self-renewal, growth and differentiation of cells within neurospheres, it is crucial that individual nuclei are accurately identified using image segmentation. Hence effective segmentation algorithm is indispensible for microscopy based neural stem cell studies. In this paper, we present a seed finding approach in scale space to identify the center of nuclei in 3-D. Then we present a novel segmentation approach, called "Evolving Generalized Voronoi Diagram", which uses the identified centers to segment nuclei in neurospheres. Comparison of our computational results to mannually annotated ground truth demonstrates that the proposed approach is an efficient and accurate segmentation approach for 3-D neurospheres.

## 1 Introduction and Background

The dogmatic concept, "adult brains are unable to make new neurons", has dominated neuroscience thinking for centuries[1] until the first challenge from Altman J. and Das G.[2], who saw cells that appeared to be newly born neurons in 1960's. Later in 1980s, Goldman S. and Nottebohm F.[3] found solid evidence that canaries give birth to waves of new brain neurons seasonally in a particular area of their brains. The discovery of *adult* neural stem cells (NSCs) opens the door to potential treatments for neurological diseases, such as Parkinsons and Alzheimers, by endogenous repair. To be able to utilize NSCs for therapy and investigations of neurodevelopment we need to have a better understanding of their cell biology. There are no definitive markers for NSCs and they are normally followed by functional critiera[5] including; (a) self-renewal ability to passage for many generations, (b) multipotency ability to generate neurons, astrocytes and oligodendrocytes and (c) to regenerate brain tissue. Our understanding of NSCs and their therapeutic potential relies on propagating these cells *in vitro*. One

G. Bebis et al. (Eds.): ISVC 2009, Part I, LNCS 5875, pp. 531–543, 2009.

of the most popular functional assays for NSCs is the *Neurosphere Formation Assays* (NFAs). It provides a relatively simple and robust means to investigate the propagation of NSCs. Although the exact relationship between NSCs and NFAs is unclear yet[4], NFAs remain a good evidence of the presence of NSCs[5].

Fluorescence microscopy is a common, probably preeminent, tool to understand the cell biology of NSCs. Automated analysis of the acquired 3-D images is critical to identify the stem cells within neurospheres based on their activities and behaviors. In order to do so, we need to accurately identify and segment each nucleus from the neurosphere, however, it is challenging since the nuclei are morphologically diverse and usually clumpy with each other. Using simple approaches, such as thresholding or watershed, will cause severe under-segmentation or over-segmentation. One way to solve this segmentation problem is to first find the centers of the nuclei, which we call *seed finding* in this paper, and then perform some kind of flooding or region-growing from the seeds to segment the nuclei. Traditionally, the centers of the nuclei are identified as local maxima in the distance transform of binary or gray level images. This approach works well only when the shapes of nuclei are ellipsoidal or spherical and their sizes are homogeneous. However, these two conditions are satisfied in few biological experiments. More sophisticated approaches are needed, for example, fast radial symmetry transform[6] and phase symmetry approach[7,8]. More recently, an iterative voting approach of radial symmetries based on the gradient direction is presented in [9] for inferring the center of objects. This approach is applied to identify the center of closely packed cells in 2-D images in [10] and then it is extended to identify the center of nuclei in 3-D mammosphere images in [11]. Another seed detection approach based on Laplacian of Gaussian filter is applied on 2-D gray level images in [12].

Seed finding is only the first step of nuclei segmentation. Many segmentation approaches have been reported. The distance transform and a modified watershed approach are applied in [14] to segment the nuclei in 3-D microscopy images of *C.elegans*. Most of the nuclei can be correctly segmented by the proposed approach, however post-processing may be needed to further split or merge objects[14]. A gradient flow and local adaptive thresholding approach for 3-D nuclei segmentation is presented[15] and tested on both synthetic images and real images. The combination of level set and watershed approach is also popular, for example [16]$\sim$[17]. In order to overcome over-segmentation and under-segmentation, different topological constraints are exploited, such as topological dependence[18,19], simple point concept[20] and topology-preserving model[21]. An important concept is proposed in [18]: image intensity and geometrical shape of the objects are both important cues for an accurate segmentation. It is difficult to include all important work in this short paper. Other related work can be found, such as the flexible contour model[22] and ellipse detector[23].

For the rest of the paper, we describe the preparation of biological samples and the microscope configurations in Section 2. In Section 3, we first present the pre-processing of 3-D images. Then a seed finding approach is presented to identify the center of nuclei by searching the local maxima in scale space

representations of the distance transform of binary images. Section 4 proposes a novel algorithm,called "Evolving Generalized Voronoi Diagram", to segment the clumpy nuclei with irregular shapes. The experimental results and validation are presented in Section 5 followed by discussions and conclusions in Section 6.

## 2 Image Acquisition

The cells in our study are Neural Stem/Progenitor Cells derived from mouse embryo stage (E 14.5). Cells were cultured in growth media containing Epidermal Growth Factor and N2 (a growth supplement). Cells were nucleofected with plasmid Plasma Membrane Targeted-YFP (PMT-YFP) and allowed to grow in an incubator at 37°C and 5% $CO_2$ for 4-5 days to form neurospheres. At the end of 5 days, Hoechst was added to stain the nuclei and incubated for 10-15 mins before imaging. We used the Olympus confocal FV1000 for imaging. 488nm laser set at 5% power (0.86mw) was used to image PMT-YFP and 405nm laser set at 2% power (0.12mw) was used to image Hoechst. Images were acquired with a $z$ step of 0.2$\mu$m. The resolution of $x$ and $y$ axis is 0.25$\mu$m. The photomultiplier tube voltage in the confocal was set based on the signal from the sample. A 60× water immersion lens with a numerical aperture of 1.2 was used. The 3-D images contain two channels: green for PMT-YFP and blue for Hoechst. A representative neurosphere image from two different viewing angles is shown in Fig. 1.

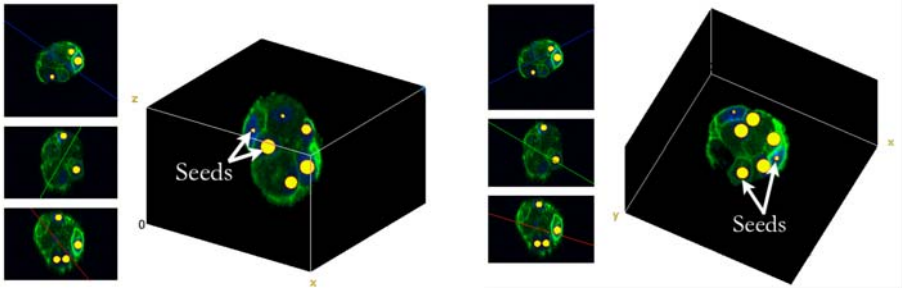


**Fig. 1.** Original 3-D Neurosphere Image and Seed Finding in Scale Space. Two different views of the original 3-D image are illustrated. The identified seeds are annotated by the arrows. The seeds are dilated by a ball structuring element of 7 voxel radius for the purpose of visualization. The apparent size of dot indicates its relative depth to the observer.

## 3 Image Pre-processing and Seed Finding

### 3.1 Image Pre-processing

The images in this paper are defined on a finite subset of three-dimensional Euclidean space, $\mathbf{\Theta} \subset \mathbb{R}^3$. A point $\vec{r}$ in $\mathbf{\Theta}$ is represented by Cartesian coordinate,

*e.g.* $\vec{r} = (x, y, z) \in \mathbf{\Theta}$. $f^n(\vec{r}) : \mathbf{\Theta} \mapsto \mathbb{R}$ and $f^c(\vec{r}) : \mathbf{\Theta} \mapsto \mathbb{R}$ represent the intensities of Hoechst (blue) and PMT-YFP (green) at $\vec{r}$, respectively. The superscripts "$n$" and"$c$" indicate "nucleus" and "cell". The image intensities are normalized such that $f^n(\vec{r}) \in [0, 1]$ and $f^c(\vec{r}) \in [0, 1]$.

Both $f^n(\vec{r})$ and $f^c(\vec{r})$ contain important information for the 3-D nuclei segmentation. In order to avoid photobleaching and phototoxicity for the live cells, fast scanning speed is applied, *i.e.* 2m$s$/voxel, which limits the achievable signal-to-noise ratio. Image enhancements such as histogram equalization and contrast improvement are applied to $f^n(\vec{r})$ and $f^c(\vec{r})$ and produce $\tilde{f}^n(\vec{r})$ and $\tilde{f}^c(\vec{r})$, respectively. As shown in Fig. 1, the value of $f^c(\vec{r})$ is relatively high (bright) at the cell boundary. Thus, we combine these two images into one image:

$$f(\vec{r}) = \tilde{f}^n(\vec{r}) - \tilde{f}^c(\vec{r}) \tag{1}$$

The combination will make $f(\vec{r})$ darker near the cell boundaries. This facilitates the subsequent processing. Then $f(\vec{r})$ is converted to a binary image according to Otus threshold[24]. The binary image contains two regions, the background $\Omega_b$ and the foreground $\Omega_f$ with $\Omega_b \cup \Omega_f = \mathbf{\Theta}$ and $\Omega_b \cap \Omega_f = \emptyset$. Then the distance transform is applied:

$$D(\vec{r}) = \min_{\vec{r'} \in \Omega_b} |\vec{r} - \vec{r'}| \tag{2}$$

where the distance between the two point $\vec{r}$ and $\vec{r'}$ is the Euclidean distance: $|\vec{r} - \vec{r'}| = \sqrt{(x - x')^2 + (y - y')^2 + (z - z')^2}$. It is obvious that if $\vec{r} \in \Omega_b$, $D(\vec{r}) = 0$, otherwise, $D(\vec{r}) > 0$.

### 3.2 Seed Finding in Scale Space

Segmentation of the nuclei in neurospheres is very challenging, because they are closely packed and touch each other. Hence, finding the centers of the nuclei, known as *seed finding*, is a critical step to assist our subsequent processing. The distance transform given in Eq.(2) can identify the seeds nicely, provided the sizes of the nuclei are similar and their shapes are spherical or ellipsoidal. Unfortunately, these two conditions can not be satisfied in our study. The results of using the distance function directly are very sensitive to the thresholding value, which is used to identify the local maxima. If smaller nuclei are detected, then the seeds of bigger nuclei may merge due to irregular shapes; on the other hand, if bigger nuclei are successfully separated, it is very likely that some smaller nuclei are undetected.

In order to overcome these challenges, we present a robust method based on scale space theory[25], which can be used to identify centers of objects with different sizes. It is also applied to identify the stable key points in [13]. It has been shown by [25] and [26] that under a variety of reasonable assumptions, Gaussian kernel is the only scale-space kernel. The 3-D Gaussian kernel of width $\sigma$ is given by:

$$G(\vec{r},\sigma^2)=\frac{1}{\sqrt{(2\pi\sigma)^3}}\exp\left(-\frac{|\vec{r}|^2}{2\sigma^2}\right) \tag{3}$$

where $|\vec{r}|=\sqrt{x^2+y^2+z^2}$.

For a given scale $\sigma$, the scale-space representation of distance function $D(\vec{r})$ is given as:

$$L(\vec{r},\sigma^2)=D(\vec{r})*G(\vec{r},\sigma^2) \tag{4}$$

where "$*$" means convolution. A straightforward way to obtain a multi-scale detector with automatic scale selection is to consider the normalized scale Laplacian operator. Lindeberg T. showed that the normalization of the Laplacian with the factor $\sigma^2$ is required for true scale invariance[25]. In detailed experimental comparisons[27] , it is found that the maxima and minima of scale-normalized Laplacian of Gaussian produce the most stable image features. In practice, the difference-of-Gaussian ($DoG$) provides a good approximation of the scale-normalized Laplacian of Gaussian. The $DoG$ can be efficiently calculated according to:

$$\begin{aligned} DoG(\vec{r},\sigma^2) &= \frac{1}{2\Delta\sigma^2}(G(\vec{r},\sigma^2+\Delta\sigma^2)-G(\vec{r},\sigma^2-\Delta\sigma^2))*D(\vec{r}) \\ &= \frac{1}{2\Delta\sigma^2}(L(\vec{r},\sigma^2+\Delta\sigma^2)-L(\vec{r},\sigma^2-\Delta\sigma^2)) \end{aligned} \tag{5}$$

where $2\Delta\sigma^2$ is a positive normalization factor, which is essential to achieve the scale invariant representation of the $DoG$. In order to identify the seeds, we find the local maxima of $DoG(\vec{r},\sigma^2)$:

$$(\tilde{\vec{r}},\tilde{\sigma}^2)=arg\ \text{local-max}_{(\vec{r},\sigma^2)}\left[DoG(\vec{r},\sigma^2)\right] \tag{6}$$

The identified local maximum voxel $\tilde{\vec{r}}$ is the center of the nuclei, *i.e.* the *seeds*. We denote them by $s_i$ $(i=1,2,..N)$, where $N$ is the number of seeds. The convolution of $D(\vec{r})$ at different scales will also partially solve the problem associated with irregular nuclei shape. Two different views of an original image are illustrated in Fig. 1. As shown in Fig. 1, the dots annotated by the arrows illustrate the detected seeds using our approach. Note that the size of dot indicates its relative depth to the observer. The detected seeds can successfully represent the center of nuclei of different sizes and irregular shapes.

## 4 Nuclei Segmentation Based on Evolving Generalized Voronoi Diagram

The nuclei segmentation is not only to simply separate the nuclei from the background, but also separate them from each other. Inspired by the concept of topological dependence[18,19], we present our algorithm of "Evolving Generalized Voronoi Diagram" (EGVD) to segment the 3-D nuclei. In this algorithm, we

evolve the level set function using Chan-Vese method introduced in [18]. At each iteration of level set evolution, we prevent splitting and merging of the objects using Generalized Voronoi Diagram. We followed the idea introduced in [18,19] and modified the distance transform $D(\vec{r})$ based on the identified seeds:

$$\bar{D}(\vec{r}) = \begin{cases} 1 & \text{if } \vec{r} \in \bigcup_{i=1}^{N} s_i \\ \frac{D(\vec{r})}{\max(D(\vec{r}))} & \text{otherwise} \end{cases} \tag{7}$$

Then initialization of the level set is given by [18,19]:

$$\phi^{t=0}(\vec{r}) = \bar{D}(\vec{r}) - 1 \tag{8}$$

such that active contours are initialized at the found seeds in Section 3.2. We evolve the level set function based on the formulation given in [18,19]:

$$\phi^{t+\Delta t} = \phi^t + \Delta t \cdot \delta_\epsilon(\phi^t)[-\lambda_1(D(\vec{r}) - c_1)^2 + \lambda_2(D(\vec{r}) - c_2)^2] \tag{9}$$

where the constants $c_1$ and $c_2$ are the mean values of the background and foreground.

For numerical stability reasons, the level set function is usually reinitialized to be the distance function after a few iterations. This is particularly important when the level set curvature term $div(\frac{\nabla\phi}{|\nabla\phi|})$ is present in the level set updating. In this paper, we did not do so, but still achieved numerical stabilities for the following two reasons. Firstly, the length parameter $\nu$ is zero in Eq. (9) by [18,19] so that the level set curvature term is absent. Secondly, using a regularized delta function $\delta_\epsilon(\phi^t)$ with a large $\epsilon$, ($\epsilon = 1.0$) contributed to maintaining the numerical stability.

Evolving the level set using Eq.(9) is insufficient to segment the nuclei correctly. We develop the EGVD algorithm to prevent objects from splitting and merging. Before we present our algorithm, two important definitions are needed: *Generalized Voronoi Diagram*(GVD) and *Choice Function*. Let $\omega_i^{n,t}$ $(i = 1, 2, ...N)$ denote nuclei segments at artificial time step $t$. They are defined as follows:

**Generalized Voronoi Diagram:** *Given a set of disjoint connected regions $\omega_i^{n,t}$ for $i = 1, 2, ...N$ with $\omega_i^{n,t} \cap \omega_j^{n,t} = \emptyset\ \forall i \neq j$, define the Generalized Voronoi Diagram (GVD) as $V_i(\omega_1^{n,t}, \omega_2^{n,t}, ...\omega_N^{n,t})$ corresponding to each $\omega_i^{n,t}$:*

$$V_i(\omega_1^{n,t}, \omega_2^{n,t}, ...\omega_N^{n,t}) = \left\{ \vec{r} \in \mathbf{\Theta} | \min_{\vec{s} \in \omega_i^{n,t}} |\vec{r} - \vec{s}| < \min_{\vec{s'} \in \cup_{j \neq i}^{N} \omega_j^{n,t}} |\vec{r} - \vec{s'}| \right\} \tag{10}$$

**Choice Function:** *Given a connected region $s_i$ as seeds, and a set of points $\mathbf{\Gamma}$. $\mathbf{\Gamma}$ may consist of several connected regions. Define the choice function, also known as selector, $\mathcal{C}(\mathbf{\Gamma}|s_i)$ that chooses the connected region from $\mathbf{\Gamma}$ which contains $s_i$ . $\mathcal{C}(\mathbf{\Gamma}|s_i)$ returns empty set $\emptyset$, if $s_i \not\subset \mathbf{\Gamma}$*

Based on the above definitions, our Evolving Generalized Voronoi Diagram algorithm is given as follows:

1. Find the seeds to obtain $s_i$, $(i = 1, 2, ...N)$ according to Eq. 6.
2. Initialize the level set function for the nuclei segmentation according Eq. (8).
3. Update the level set function $\phi^t \rightarrow \phi^{t+\Delta t}$ using Eq. (9). Then update the *GVD* regions iteratively at each time step $t+\Delta t$ to obtain $\omega_i^{n,t+\Delta t}$ as follows:
   (a) Let $\Omega^{n,t+\Delta t} = \{\vec{r} \in \mathbf{\Theta} | \phi^{t+\Delta t} \geq 0\}$.
   (b) Define $\bar{\omega}_{i,k=0}^{n,t+\Delta t} = \omega_i^{n,t}$, for $i = 1, 2, ...N$. $k$ is used to index successive estimates of nuclei segments at $t + \Delta t$.
   (c) For each $i = 1, 2, ...N$, calculate *GVD*: $V_i(\bar{\omega}_{1,k}^{n,t+\Delta t}, \bar{\omega}_{2,k}^{n,t+\Delta t}, ...\bar{\omega}_{N,k}^{n,t+\Delta t})$ and update the nuclei segment using the choice function:

$$\bar{\omega}_{i,k+1}^{n,t+\Delta t} = \mathcal{C}(\Omega^{n,t+\Delta t} \cap V_i(\bar{\omega}_{1,k}^{n,t+\Delta t}, \bar{\omega}_{2,k}^{n,t+\Delta t}, ...\bar{\omega}_{N,k}^{n,t+\Delta t}) | s_i) \tag{11}$$

   and then set $k \rightarrow k + 1$.
   (d) Iterate step 3(c) until convergence, i.e. $\bar{\omega}_{i,k+1}^{n,t+\Delta t} = \bar{\omega}_{i,k}^{n,t+\Delta t}$
   (e) Set $\omega_i^{n,t+\Delta t} \leftarrow \bar{\omega}_{i,k+1}^{n,t+\Delta t}$ . This completes the update of GVD and nuclei segments at $t + \Delta t$.
4. Repeat step 3 until convergence of the level set function.

In Fig. 2, we present an illustration in 2-D for better understanding. Our algorithm consists of an outer loop for level set evolution and an inner loop for EGVD. GVDs define the boundary of nucleus segments where two level set segments might merge. Essentially, EGVD algorithm involves a series of fine adjustment of the intermediate GVDs. Suppose at time $t$, $\omega_i^{n,t}$ are obtained and $V_i$ is calculated based on Eq.(10). At the next time step $t + \Delta t$, the level set function is updated and a new $V_i$ is needed to give correct $\omega_i^{n,t+\Delta t}$. We first use the $V_i$ calculated at the previous time step, illustrated by shaded area in Fig. 2(a), as initial GVD for the inner loop iteration. Given GVD and $s_i$, we use the choice function to calculate a connected region for each nucleus, as shown by the dotted regions in Fig. 2(b). Then a new GVD is calculated based on these dotted regions, as shown by the shaded area in Fig. 2(c). The process of evolving GVD is performed iteratively until GVD does not change anymore, which will be the final GVD in this time step. As we can see from Fig. 2(d), the nucleus in $V_j$ has converged in this iteration. It can be proven that the EGVD algorithm converges, while we shall leave its rigorous mathematical proof for further publication due to the limitation of space.

Comparing with existing approaches, EGVD algorithm has a few advantages. First of all, EGVD is conceptually very simple. Comparing with the maximum common boundary criterion in [18,19], it does not require the considerations of many different cases in which the level set function split and merge. EGVD is also fast and efficient. It is not necessary to determine whether a given point is a simple point[20]. EGVD is more flexible than the formulation introduced in [21], in which any topological change is forbidden. EGVD only disallows splitting and merging, while it tolerates other topological changes, such as adding a hole. Lastly, it is trivial to extend EGVD to other dimensions.

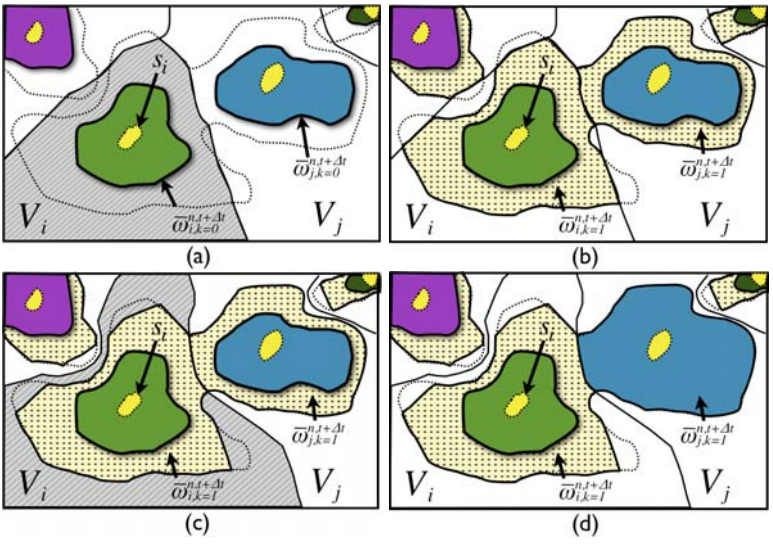


**Fig. 2.** Evolving the Generalized Voronoi Diagram. Central regions annotated by $s_i$ are the identified seeds. The shaded regions in (a) and (c) are corresponding $V_i$ for $\bar{\omega}_{i,k=0}^{n,t+\Delta t}$ and $\bar{\omega}_{i,k=1}^{n,t+\Delta t}$. The dotted regions represent the different $\bar{\omega}_{i,k}^{n,t+\Delta t}$ at different iterations before convergence.

## 5 Experimental Results

Two of our segmentation results are shown in Fig. 3. We use random colors to represent different nuclei. Although the nuclei are clumpy and touch each other in the neurosphere, our EGVD algorithm is able to segment them satisfactorily.

Quantitative validation is an important and necessary step to evaluate the accuracy of algorithms. We select eight 3-D Neurosphere images and manually create the ground truth using a touch screen laptop and "Segmentation Editor" in Fiji [1]. The boundary of each nucleus is labelled manually from the top to bottom. Segmentation Editor has the function of 3-D interpolation and we don't need to draw the boundary at each image slice. The interval of the boundary drawing is 3∼7 slices depending on the shape of the nuclei. A few slices of a ground-truth image are shown in Fig. 4. The masks are the created nucleus segments. The boundaries of a nucleus, annotated by the arrows in Fig. 4 (b)∼(h), are drawn manually according to best human perception.

Based on the ground truth, there are *246* nuclei in eight 3-D images. For a given image, let $\omega_i^g, i = 1, 2, ...N$ denote the objects of the ground truth and $\omega_i^s, i = 1, 2, ...M$ denote the computational objects given by EGVD approach. We define a score $\alpha_i$ to describe accuracy of the computational results, which is

[1] Fiji package with Segmentation Editor is available at: http://pacific.mpi-cbg.de

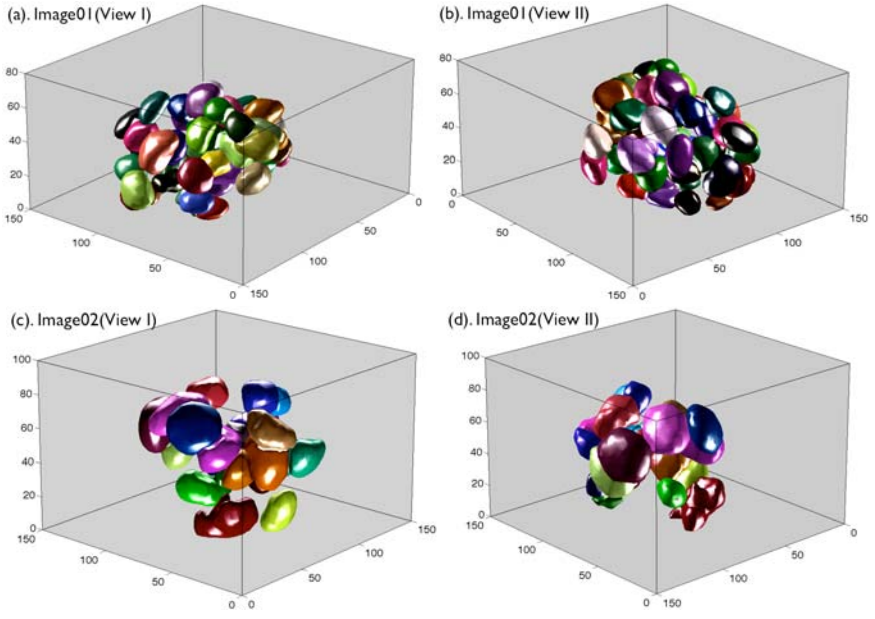


**Fig. 3.** Segmented Nuclei in 3-D. (a) and (b) display two different views of the segmented nuclei in Image01. (c) and (d) illustrate the segmentation results of Image02. Random color is selected to represent each nucleus.

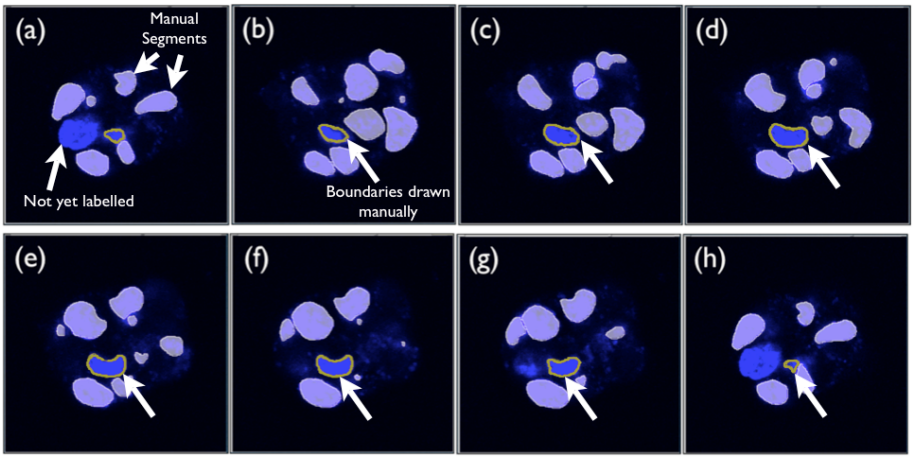


**Fig. 4.** The Procedure of Ground Truth Labeling. The nuclei segments are the manually created. The contours annotated by the arrows represent boundaries of a nucleus. They are drawn manually according to the best human perception. The boundaries in the slices between them will be interpolated by the Segmentation Editor.

$$\alpha_i = \max_j \left( \frac{|\omega_i^s \cap \omega_j^g|}{|\omega_i^s \cup \omega_j^g|} \right) \tag{12}$$

where $|\cdot|$ means the volume of the given connected component. It is obvious that $\alpha_i \in (0, 1)$. If a computational object perfectly matches a ground truth object, $\alpha_i$ is 1.0; while $\alpha_i = 0$ when $\omega_i^s$ does not overlap any $\omega_j^g$. On the other hand, it is also possible that some $\omega_j^g$ does not overlap any $\omega_i^s$, which we called Missing Segments.

In order to test the performance of EGVD when seeds are correctly provided, we use the geometrical center of the ground truth objects as seeds and then apply EGVD approach to segment nuclei. We also use the proposed approach in scale space with different $\sigma$ to detect the seeds and then compare our computational results with ground truth. The probability distribution of score $p(\alpha)$ and $P(\alpha) = \int_\alpha^1 p(\alpha')d\alpha'$ are shown in Fig. 5. From this figure, we can see that the Missing Segments caused a small peaks near $\alpha = 0$ in $p(\alpha)$, while the falsely detected seeds caused under-segmentation or over-segmentation and thus produced the small peaks near $\alpha = 0.5$ in $p(\alpha)$. From the curves of $p(\alpha)$ given different $\sigma$, we know there is a optimal value of $\sigma$ for nuclei segmentation. The numbers of seeds identified by different $\sigma$ are indicated in legend. It is clear that the number of detected seeds does not necessarily imply better performance, because some of them might be positioned inaccurately. The strong peaks near $\alpha = 0.9$ in the curves of $p(\alpha)$ indicate that majority of the nuclei are satisfactorily segmented. The mean segmentation accuracy of EGVD given real seeds is about 75% and it is about 70% given $\sigma = 2.1$ for seed finding.

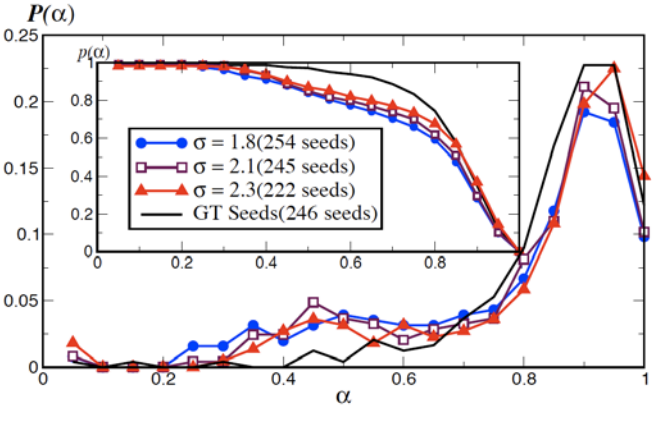


**Fig. 5.** Performances of EGVD Algorithm. The probability distribution function $p(\alpha)$ and corresponding $P(\alpha)$ are illustrated. If seeds are correctly provided, EGVD can segment majority of nuclei nicely indicated by the peak near $\alpha = 0.9$. The average segmentation accuracy is 75%. Using our seed finding approach, the falsely detected seeds caused the small peaks near $\alpha = 0.5$ in $p(\alpha)$.

## 6 Discussions and Conclusions

A seed finding approach in scale space and a novel segmentation algorithm, Evolving Generalized Voronoi Diagram (EGVD), are proposed to segment the nuclei in neurosphere. Our study combines careful image acquisition with dual dyes for nuclear and membrane labelling, and robust image analysis to use the data optimally. In order to quantitatively evaluate our proposed approaches, we create the ground truth of eight 3-D images containing *246* nuclei.

The computational results demonstrate that the EGVD algorithm can satisfactoryly segment the nuclei in neurospheres if the seeds are provided accurately. Our seed finding approach is validated by comparing the computational results with the ground truth. The results demonstrate our seed finding approach can identify most of the seeds correctly, though there are still some errors, which might cause under-segmentation and over-segmentation, as indicated by the weak peaks near $\alpha = 0.5$ in $p(\alpha)$ in Fig. 5. A more complete study on the parameter tuning of $\sigma$ in the seed finding algorithm is needed to optimize the segmentation performance. Another possible improvement is that instead of simply using the PMT-YFP signal as in Eq. (1), we should utilize this important information more sufficiently. However, more sophisticated techniques are needed to extract the cell boundaries, since the PMT-YFP signal is not uniformly distributed near the cell boundaries and sometimes is really weak.

We expect our methods to be generally applicable to other stem cell assemblies, such as mamospheres, and more generally in the area of embryology. In the future, we plan to use the tools described to investigate in detail neurosphere development, including long range cell motion, apoptosis, and cavity formation, using 4D microscopy.

## References

1. Barinaga, M.: Newborn Neurons Search for Meaning. Science 299, 32–34 (2003)
2. Altman, J., Das, G.D.: Post-natal origin of microneurones in the rat brain. Nature 207, 953–956 (1965)
3. Goldman, S.A., Nottebohm, F.: Neuronal Production, Migration, and Differentiation in a Vocal Control Nucleus of the Adult Female Canary Brain. PNAS 80, 2390–2394 (1983)
4. Reynolds, B.A., Rietze, R.L.: Neural Stem Cells and Neurospheres – Re-evaluating the Relationship. Natural Methods 2, 333–336 (2005)
5. Louis, S.A., Rietze, R.L., Deleyrolle, L., Wagey, R.E., Thomas, R.E., Eaves, R.E., Reynolds, B.A.: Enumeration of Neural Stem and Progenitor Cells in the Neural Colony-forming Cell Assay. Stem Cell 26, 988–996 (2008)
6. Loy, G., Zelinsky, A.: Fast Radial Symmetry for Detecting Points of Interest. IEEE Trans. on PAMI 25, 959–973 (2003)
7. Kovesi, P.: Image Features From Phase Congruency. Videre: A Journal of Computer Vision Research 1, 2–26 (1999)
8. Kovesi, P.: Phase Congruency: A Low-level Image Invariant. Psychological Research Psychologische Forschung 64, 136–148 (2000)

9. Yang, Q., Parvin, B.: Perceptual Organization of Radial Symmetries. In: Proceedings of CVPR, vol. 1, pp. 320–325 (2004)
10. Raman, S., Parvin, B., Maxwell, C., Barcellos-Hoff, M.H.: Geometric Approach to Segmentation and Protein Localization in Cell Cultured Assays. In: Bebis, G., Boyle, R., Koracin, D., Parvin, B. (eds.) ISVC 2005. LNCS, vol. 3804, pp. 427–436. Springer, Heidelberg (2005)
11. Han, J., Chang, H., Yang, Q., Barcellos-Hoff, M.H., Parvin, B.: 3D Segmentation of Mammospheres for Localization Studies. In: Bebis, G., Boyle, R., Parvin, B., Koracin, D., Remagnino, P., Nefian, A., Meenakshisundaram, G., Pascucci, V., Zara, J., Molineros, J., Theisel, H., Malzbender, T. (eds.) ISVC 2006. LNCS, vol. 4291, pp. 518–527. Springer, Heidelberg (2006)
12. Althoff, K., Degerman, J., Gustavsson, T.: Combined Segmentation and Tracking of Neural Stem-Cells. In: Kalviainen, H., Parkkinen, J., Kaarna, A. (eds.) SCIA 2005. LNCS, vol. 3540, pp. 282–291. Springer, Heidelberg (2005)
13. Lowe, D.G.: Distinctive Image Features from Scale-Invariant Keypoints. International Journal of Computer Vision 60, 91–110 (2004)
14. Long, F., Peng, H., Myers, E.: Automatic Segmentation of Nuclei in 3D Microscopy Images of C. elegans. In: Proceedings of ISBI 2007, pp. 536–539 (2007)
15. Li, G., Liu, T., Tarokh, A., Nie, J., Guo, L., Mara, A., Holley, S., Wong, S.T.C.: 3D Cell Nuclei Segmentation Based on Gradient Flow Tracking. BMC Cell Biology 8 (2007), http://www.biomedcentral.com/1471-2121/8/40
16. Tai, X., Hodneland, E., Weickert, J., Bukoreshtliev, N.V., Lundervold, A., Gerdes, H.: Level Set Methods for Watershed Image Segmentation. In: Sgallari, F., Murli, A., Paragios, N. (eds.) SSVM 2007. LNCS, vol. 4485, pp. 178–190. Springer, Heidelberg (2007)
17. Yan, P., Zhou, X., Shah, M., Wang, S.T.C.: Automatic Segmentation of High-throughput RNAi Fluorescent Cellular Images. IEEE Transaction on Information Technology in Biomedicinel 12, 109–117 (2008)
18. Yu, W.M., Lee, H.K., Hariharan, S., Bu, W.Y., Ahmed, S.: Level Set Segmentation of Cellular Images Based on Topological Dependence. In: Bebis, G., Boyle, R., Parvin, B., Koracin, D., Remagnino, P., Porikli, F., Peters, J., Klosowski, J., Arns, L., Chun, Y.K., Rhyne, T.-M., Monroe, L. (eds.) ISVC 2008, Part I. LNCS, vol. 5358, pp. 540–551. Springer, Heidelberg (2008)
19. Yu, W.M., Lee, H.K., Hariharan, S., Bu, W.Y., Ahmed, S.: Quantitative Neurite Outgrowth Measurement Based on Image Segmentation with Topological Dependence. Cytometry Part A 75A, 289–297 (2009)
20. Xiao, H., Chenyang, X., Jerry, L.P.: A Topology Preserving Deformable Model Using Level Sets. In: Proceeding of CVPR, vol. 2, pp. 765–770 (2001)
21. Le Guyader, C., Vese, L.A.: Self-Repelling Snakes for Topology-Preserving Segmentation Models. IEEE Transactions on Image Processing 17(5), 767–779 (2008)
22. Clocksin, W.F.: Automatic Segmentation of Overlapping Nuclei with High Background Variation Using Robust Estimation and Flexible Contour Model. In: Proceedings of ICIAP, vol. 17, pp. 682–687 (2003)
23. Yap, C.K., Lee, H.K.: Identification of Cell Nucleus Using a Mumford-Shah Ellipse Detector. In: Bebis, G., Boyle, R., Parvin, B., Koracin, D., Remagnino, P., Porikli, F., Peters, J., Klosowski, J., Arns, L., Chun, Y.K., Rhyne, T.-M., Monroe, L. (eds.) ISVC 2008, Part I. LNCS, vol. 5358, pp. 582–593. Springer, Heidelberg (2008)
24. Otsu, N.: A Threshold Selection Method from Gray-level Histograms. IEEE Transactions on Systems, Man & Cybernetics 9, 62–66 (1979)

25. Lindeberg, T.: Scale-space Theory: A Basic Tool for Analysing Structures at Different Scales. Journal of Applied Statistics 21(2), 224–270 (1994)
26. Koenderink, J.J.: The Structure of Images. Biological Cybernetics 50, 363–396 (1984)
27. Mikolajczyk, K., Schmid, C.: An Affine Invariant Interest Point Detector. In: Heyden, A., Sparr, G., Nielsen, M., Johansen, P. (eds.) ECCV 2002. LNCS, vol. 2350, pp. 128–142. Springer, Heidelberg (2002)